2015 Tenth International Conference on Ecological Vehicles and Renewable Energies (EVER)

Infuence of Rotor Geometry on NVH Behavior of Synchronous Reluctance Machine

Fabien Chauvicourt, Cassio Faria
LMS Engineering RTD
Siemens Industry Software NV
Leuven, Belgium
fabien.chauvicourt@siemens.com

Arkadiusz Dziechciarz, Claudia Martis
Technical University of Cluj-Napoca
28 Memorandumului
Cluj-Napoca, Romania
arkadiusz.dziechciarz@mae.utcluj.ro

***Abstract*— High prices of permanent magnets (PM), in Permanent Magnet Synchronous Machines of current electric vehicles, pushes for the development of reluctance machines. Synchronous reluctance machine (SynRM) can be a competitive technology when compared to other machines, e.g. induction machines, since the lack of rotor winding limit the copper losses. In SynRM torque is produced due to anisotropy of the rotor that is achieved by introducing flux barriers in the rotor. These flux barriers have an influence on Noise Vibration and Harshness (NVH) behavior of the machine, since they are responsible for variation of magnetic resistance [1]. Torque ripple which is also higher in synchronous machines than in other types of machine causes extra vibrations and noise [2]. In this paper, the influence of flux barriers configuration on the overall NVH behavior of the machine is studied. A multi-physics numerical study also permits to do a review on NVH issues origins in SynRM .**

Keywords — Synchronous Reluctance Machine, rotor geometry, flux barriers, multi-physics model, NVH

I. INTRODUCTION

Electrical machines used in electric vehicles are required to have high efficiency and high torque at possible small installation space [3]. The torque in SynRM is produced due to rotor anisotropy [4]. This anisotropy depends on the rotor construction. The main goal while designing a machine is to obtain the highest possible saliency ratio which decides about machine's torque. In order to obtain the desired saliency ratio, the flux barriers have to be properly designed. The shape of the flux barriers influences the path of magnetic flux inside the poles. The distribution of magnetic flux affects the forces exerted on the stator which are responsible for vibrations within the machine.

It is possible that machines with high saliency ratio can at the same time have very high vibration and noise which might not be acceptable for electric drive application. This is why to obtain the required parameters of the machine, a coupled electromagnetic-vibroacoustic multi-physics design approach has been used in this paper. After defining the basic parameters of the machine such as stator/rotor number of slots/poles, number of rotor flux barriers, etc, and applying a fast pre-sizing analytical design procedure, a finite element analysis (FEA) has been performed to characterize the electromagnetic (EM) and NVH behavior of the machine.

II. ROTOR TOPOLOGIES UNDER CONSIDERATION

Three different rotor topologies are investigated in this study and are presented together with equipotential contours in Figure 1. They all are composed of four flux barriers with diverse geometries. The barriers' shapes that were chosen are very common in literature [9], [12] and are used as base shapes for further optimization of rotor structure [10], [11]. Additional information about machine's topology is given in Table 1. The first one (a) is made of four curved flux barriers while the second one (b) has more rectangular-shaped flux barriers. Although the third one (c) looks similar to the second one, the smallest sheet at the edge of the rotor pole at its mid-angle has been removed. For consistency, let us call the topologies respectively rotor 1st, rotor 2nd and rotor 3rd.

As a matter of comparison, the FEA followed exactly the same procedure and assumptions for each rotor topology. JMAG® has been the software utilized for these FEAs. The stator and rotor are considered to be made of isotropic steel named M300-35A for all topologies. Rotational speed of interest for this analysis lies in between 1600 rpm and 4800 rpm with steps of 400 rpm.

Parameter	Value
Number of stator slots	24
Air gap length	1 [mm]
Rotor's diameter	171 [mm]
Stator's outer diameter	300 [mm]

Table 1. Machine's geometry parameters

978-1-4673-6785-1/15/$31.00

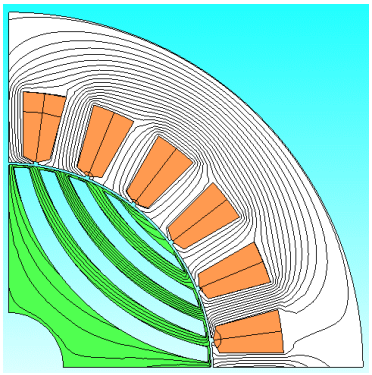

(a)

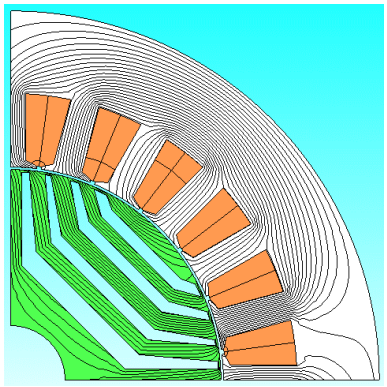

(b)

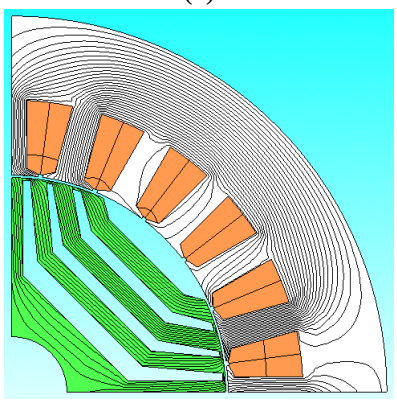

(c)

Figure 1. One pole of the 1st (a), 2nd (b) and 3rd (c) rotor topologies with equipotential contours

III. ELECTROMAGNETIC SIMULATIONS

The machine was supplied with a sinusoidal three phase current source. The nominal parameters of the machine are: $P_N = 22$ kW, $T_N = 100$ Nm, $n_N = 2100$ rpm. A 2D FEM analysis in each case was performed for 180° angle of mechanical rotation. The sampling time was set to 20 micro seconds. This choice guarantees observation of phenomena within the human audible range, since it would allow us to up to 25 kHz by satisfying the Nyquist criterion at the same time. For speed values greater than nominal speed, the current amplitude together with current angle were changed to keep the rated output power within the nominal value as illustrated in Figure 2.

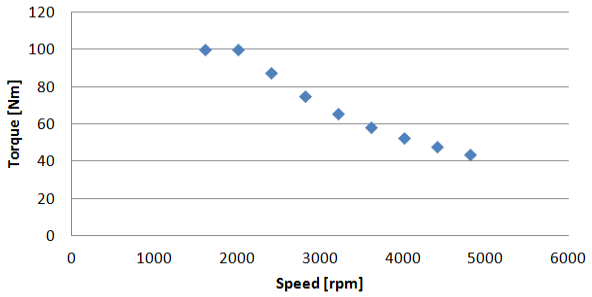

Figure 2. Torque vs. speed curve of analyzed motor

Figure 3 shows the absolute value of air gap magnetic flux density distribution along the rotor's periphery when d-axis stator magnetomotive force (MMF) was applied. In addition, Figure 4 shows the torque versus time for 4400 rpm speed case and each rotor topologies and Figure 5 shows radial forces for each topology at speed of 4400 rpm. Table 2 presents the torque ripple factor as expressed in [5] function of the rotational speed and the rotor topology.

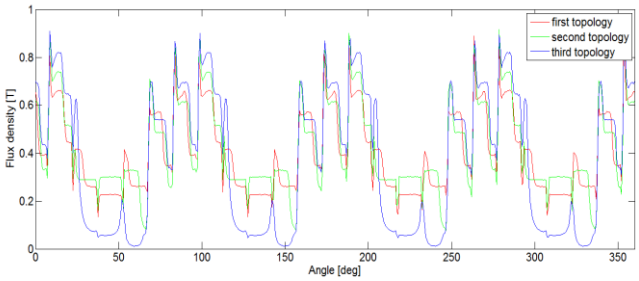

Figure 3. Air gap magnetic flux density along rotor's periphery for the first (red), the second (green) and the third (blue) rotor topology

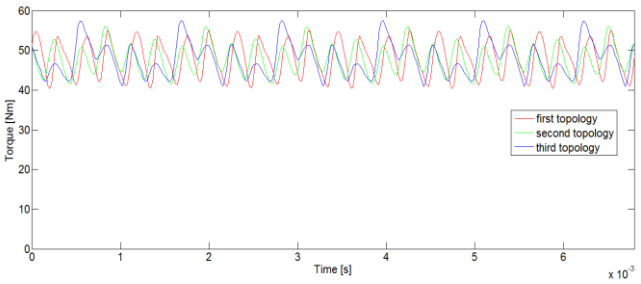

Figure 4. Output torque function of time for the first (red), the second (green) and the third (blue) rotor topology at 4400 rpm

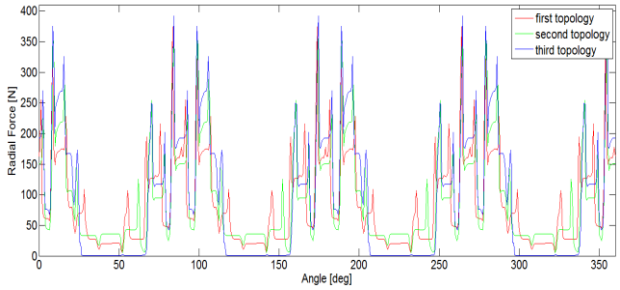

Figure 5. Radial forces for the first (red), the second (green) and the third (blue) rotor topology at 4400 rpm

One can observe that flux barriers' shape has a significant influence on magnetic flux distribution in the air gap. Likewise the torque is strongly influenced by the rotor topology and its ripple changes from one rotor to another. Overall, the 3rd rotor has higher torque ripple than the two other topologies. Those two last have slight differences in torque ripple.

rpm	Rotor 1st	Rotor 2nd	Rotor 3rd
1600	32.91%	34.88%	37.61%
2000	32.43%	34.83%	37.19%
2400	33.88%	34.47%	36.93%
2800	33.29%	32.60%	36.26%
3200	35.28%	28.53%	39.62%
3600	33.42%	34.09%	36.93%
4000	34.79%	38.95%	39.11%
4400	31.48%	30.24%	34.90%
4800	32.51%	34.19%	36.80%
Average	33.33%	33.64%	37.26%

Table 2. Torque ripple function of rotor topology and rotational speed

IV. VIBRO-ACOUSTIC ANALYSIS

A. General theory

The stator deformations are one of the main sources of vibration and noise in the SynRM. The variable magnetic field passing through each phase creates forces on stator poles. Acoustic noise comes from the pressure fluctuation imposed by the deformations of the outer surface of the motor which make the surrounding air to move. In this study, only the laminated core constituting the stator has been modeled. Therefore we neglect the effect of the housing including the cooling jacket, end windings and the end caps. Although these simulations might lead to shifted natural frequencies compared to full stator models, one can agree on going further with this assumption in the frame of rotor topologies' comparison.

The equation of motion of a generic multiple-degree-of-freedom structural system in the time-domain is described as:

$$[M]\{\ddot{x}(t)\} + [C]\{x(t)\} + [K]\{\dot{x}(t)\} = \{F(t)\} \quad (1)$$

where M, C and K are the global mass, damping and stiffness matrices respectively, $x(t)$ is the displacement at a given degree of freedom in the structure and $F(t)$ is the excitation force.

The unforced and undamped version of eq. (1) can be transformed to the Laplace domain and by considering only the imaginary part one can get to:

$$([K] - \omega^2[M])\{X(j\omega)\} = 0 \quad (2)$$

The solution of eq. (2) results in the eigenvectors/eigenmodes (Φ_n) and eigenvalues (ω^2_n). One is then able to compute an approximate forced response of (1) by using the following expression:

$$X(\omega) = \sum_{n=1}^{N} \frac{\Phi_n^T F(\omega) \Phi_n}{\omega_n^2 - \omega^2} \quad (3)$$

The acoustic radiation can then be computed in a fast and efficient way as described in [6] by:

$$\nabla^2 p(x,y,z) + k^2 p(x,y,z) = -j\rho_0 \omega q(x,y,z) \quad (4)$$

where p is the acoustic pressure at a point (x,y,z) due to a time-harmonic source distribution q at frequency ω, with the wavenumber $k = \omega/c$, c being the speed of sound and the fluid of a density of ρ_0.

B. NVH simulations performed

The FEA to get the NVH behavior of each SynRM assumed isotropic material properties of steel (M300-35A) for the stator core corresponding to: Young's modulus of 1.85e11 $N.m^{-2}$; Poisson coefficient of 0.287; and mass density of 7650 $kg.m^{-3}$. The winding effect on the mass density has not been taken into account neither the stacking factor. As mentioned in [7], these assumptions might lead to a non-negligible shift of eigenvalues. The shift of eigenfrequencies that can be noticed while using isotropic property instead of orthotropic or more accurate properties [8] has not been taken into consideration either. However, in the purpose of comparison of rotor topologies, this analysis becomes relevant.

One of the first steps of such NVH analysis is to compute the structural modes using a FEM software such as LMS Virtual.LAB®. Figure 6 shows the undeformed structural mesh together with the three main modes of the considered stator core within the frequency range of study, *i.e.* 10 to 5000 Hz. Three typical main modes appear within this frequency range and are representative of different numbers of excited lobes. Two, three and four lobes excited respectively lead the structure to deform as an egg (ovalization mode), a triangle (triangular mode) and a square (square mode).

Given the EM forces in time domain spread up on the stator surface, one is able to compute the structural forced response in the frequency domain, following eq. (3).

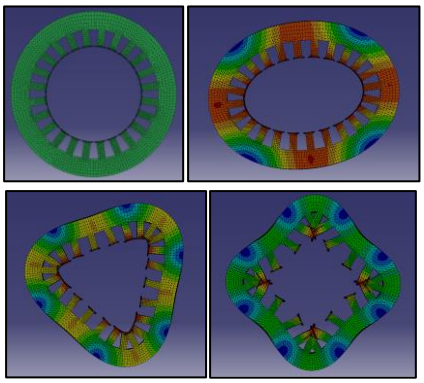

Figure 6. Structural mesh, Ovalization mode (985 Hz), Triangular mode (2559 Hz) and Square mode (4375Hz) of the stator

A mapping between the EM and the structural meshes is done in parallel with a Fast Fourier Transform (FFT) of the forces in order to link the nodes. The structural forced response (displacement) is then computed and the result is mapped to the acoustic mesh surrounding the stator. An Acoustic Transfer Vector (ATV) response case can finally be used to obtain the acoustic pressure at a chosen sink (e.g. a microphone, human ear, etc) placed 1 meter away from the stator outer surface (in the radial direction).

V. Comparison

From any rotating machine, we can expect to see so called orders. For any rotational speed, they represent the number of times a phenomenon occurs during one period of mechanical rotation. In electric motors, these orders are directly related to the number of rotor poles. One can easily derive the relationship between frequency and rotational speed for such phenomenon according to equation (5).

$$f_{\text{order n}} = \frac{N}{60} \cdot p \cdot n \qquad (5)$$

with N being the rotational speed in rpm, p the number of rotor poles (here 4) and n the number of the motor harmonic. At a specific speed case N, these orders are meant to cross the structural modes at their corresponding frequency and thus induce an amplification of the acoustic emissions i.e. resonance.

The Root Mean Square (RMS) values of acoustic pressure at a microphone located 1 m away from the stator outer surface for the rotor 1 topology (z-axis – color coded) and each rotational speed (y-axis – from 1600 rpm to 4800 rpm) are shown in Figure 7. In general, the first motor harmonic (n=1) is the one that carries most of the energy and therefore is the main contributor to the noise emitted. For this motor this phenomenon can be observed at the fourth order. This phenomenon is seen on the colormap plots (Figure 7) as the inclined green line together with the eighth order.

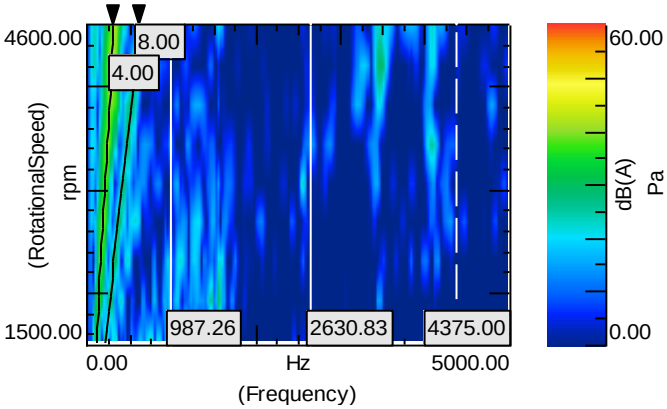

Figure 7. Acoustic pressure dB (RMS) A for the first rotor topology – frequency range 5000 Hz

The three structural modes within the frequency range of study (0 to 5 kHz) are finally not excited in the considered speed cases for each rotor topology.

The acoustic pressure levels are not very high above 2 kHz so we can assume in this study a reduced frequency range; up to 2 kHz. Figure 8 then shows the acoustic pressures for all the rotors. The order lines are displayed together with a line reminding the structural ovalization mode.

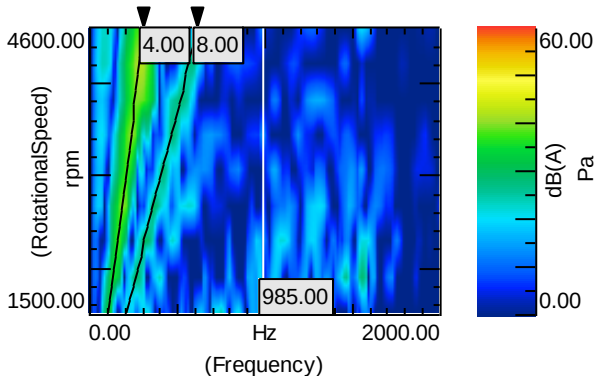

(a)

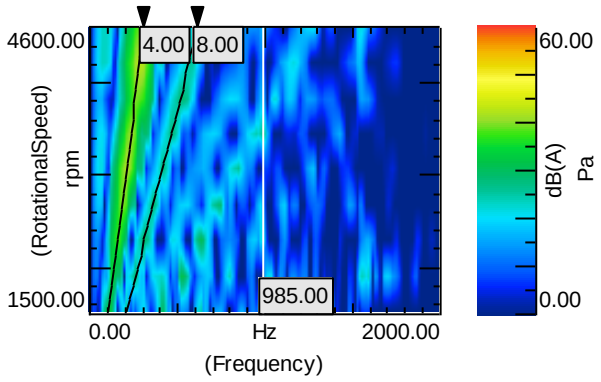

(b)

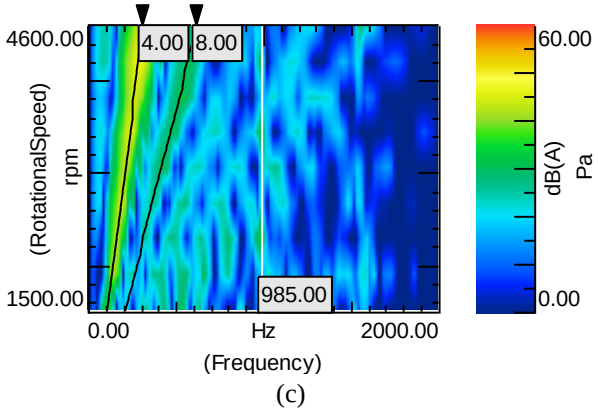

(c)

Figure 8. Acoustic pressure dB (RMS) A for the first (a) second (b) and third rotor topology – frequency range 2000 Hz

At a first glance, the 3rd rotor is to be avoided given the high levels of pressures at the 4th order (i.e. first motor harmonic). The 1st and 2nd rotor topologies are closer to each other in terms of decibels especially in the area of the 4th order.

An order cut has been performed in the interest of comparing more deeply the 1st and 2nd rotor topologies. Figure 9 shows the results for 4th and 8th order section plots which represent the first and most energy-carrier orders. Table 3 shows as well the average value of these orders for each rotor topology.

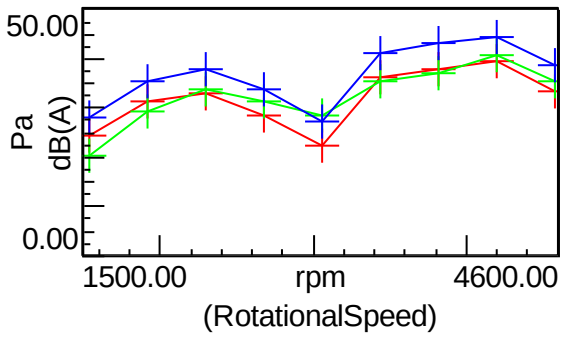

4th order section

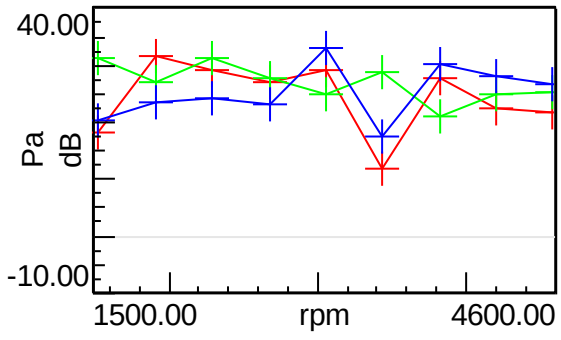

8th order section

Figure 9. Order cut for the first (red) second (green) and third (blue) rotor topology – frequency range 2000 Hz

Order	Rotor 1st	Rotor 2nd	Rotor 3rd
4th	31.8	32.5	36.6
8th	19.0	21.6	19.9

Table 3. Average acoustic pressure in RMS dB (A)

The 4th order is predominant as seen before but one is not able to conclude on the best topology between rotor 1st and 2nd by examining only this order. Indeed they have close behavior considering the 4th and 8th orders and similar average values.

Given the last results and Table 2 showing the torque ripple for each rotational speed, one is able to correlate the two of them together. Figure 10 shows that the torque ripple plays a non-negligible role in the final NVH behavior especially while looking at the 4th order. Indeed the curves' shape of torque ripple and acoustic pressure looks similar. However, no trivial relation arises from the simulations performed since several acoustic pressures do not follow exactly the torque ripple behavior.

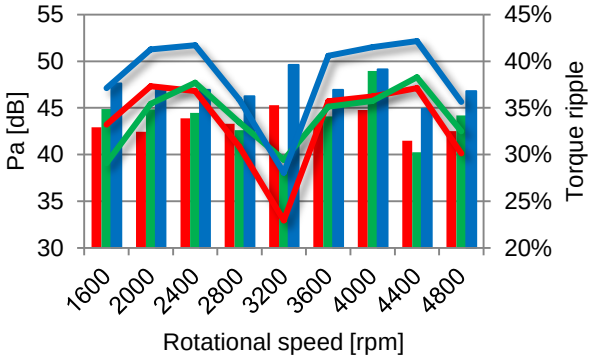

(a)

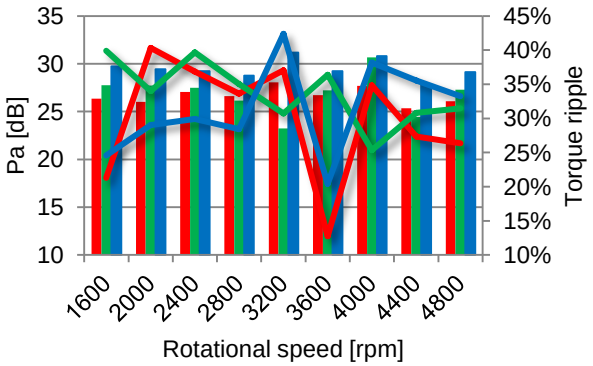

(b)

Figure 10. Order cut (lines) for 4th (a) and 8th (b) orders and torque ripple (columns) for the first (red) second (green) and third (blue) rotor topology

VI. Summary and Conlusions

In this paper, a coupled electromagnetic-vibroacoustic analysis has been presented to determine the rotor topology influence on the NVH behavior of the stator core. Using the same stator, three different rotors have been implemented in JMAG®. The EM forces calculated from this first set of simulations were inputed in LMS Virtual.LAB® to evaluate the vibro-acoustic response of the motor design.

As seen in the colormaps of Figure 8, the 3rd rotor topology is noisier than the 1st and the 2nd due to a higher overall pressure amplitudes. This result is evidence that the number of flux barriers can influence the NVH behavior of the motor. Particular to the case under investigation, a lower number of flux barriers increased the acoustic radiation of the motor.

By taking a closer look into a 4th order section of the waterfall plots, Figure 9, one can conclude that the 1st rotor is quieter than the 2nd one. The average acoustic pressure given in table 3 also corroborates with this same conclusion. One possible explanation is that a more circular and regular geometry of the flux barriers would result in better NVH behavior.

Finally, it has also been demonstrated that the rotor geometry has an impact on the air gap magnetic flux density and thus the torque ripple. A comparison between the values in table 2 and table 3 clearly indicates that a higher torque ripple results in a higher acoustic radiation by the motor but no trivial relationship could be established to relate the two, i.e. Figure 10.

Aknowledgment

This paper is part of the ADvanced Electric Powertrain Technology (ADEPT) project which is an EU funded Marie Curie ITN project, grant number 607361. Within ADEPT a virtual and hardware tool are created to assist the design and analysis of future electric propulsions. Especially within the context of the paradigm shift from fuel powered combustion engines to alternative energy sources (e.g. fuel cells, solar cells, and batteries) in vehicles like motorbikes, cars, trucks, boats, planes. The design of these high performance, low cost and clean propulsion systems has stipulated an international cooperation of multiple disciplines such as physics, mathematics, electrical engineering, mechanical engineering and specialisms like control engineering and safety. By cooperation of these disciplines in a structured way, the ADEPT program provides a virtual research lab community from labs of European universities and industries [13]. It is also important to recognize JSOL Corporation for the JMAG® licenses made available to the authors and to Siemens Industry Software for the access to LMS Virtual.LAB®.

References

[1]. Masayuki Sanada, Member, IEEE, Kenji Hiramoto, Shigeo Morimoto, Member, IEEE, and Yoji Takeda, Member, IEEE, "Torque Ripple Improvement for Synchronous Reluctance Motor Using an Asymmetric Flux Barrier Arrangement", IEEE Transactions On Industry Applications, Vol. 40, No. 4, July/August 2004

[2]. Jung Min Park, Sung Il Kim, Jung Pyo Hong and Jung Ho Lee, "Rotor Design on Torque Ripple Reduction for a Synchronous Reluctance Motor With Concentrated Winding Using Response Surface Methodology", IEEE Transactions On Magnetics, Vol. 42, No. 10, October 2006

[3]. Thomas Finken and Kay Hameyer, "Design of Electric Motors for Hybrid- and Electric-Vehicle Applications", 2009

[4]. A. Vagati, Fellow, IEEE, B. Boazzo, P. Guglielmi, Member, IEEE, G. Pellegrino, Member, IEEE, "Ferrite Assisted Synchronous Reluctance Machines: a General Approach", ICEIMach, 2012

[5]. K. T. Chau, Senior Member, IEEE, Qiang Sun, Ying Fan, "Torque Ripple Minimization of Doubly Salient Permanent-Magnet Motors", 2005

[6]. Fábio L. M. dos Santos, Jan Anthonis, Francesco Naclerio, Johan J. C. Gyselinck, "Multiphysics NVH Modeling: Simulation of a Switched Reluctance Motor for an Electric Vehicle", IEEE Transactions On Industrial Electronics, January 2014

[7]. M. van der Giet, K. Kasper, R.W. De Doncker, K. Hameyer, "Material parameters for the structural dynamic simulation of electric machines", IEEE Electrical Machines (ICEM), September 2012

[8]. Miha Pirnat, Gregor Čepon, Miha Boltezar, "Introduction of the linear contact model in the dynamic model of laminated structure dynamics: an experimental and numerical identification", Mechmachtheory, 2013

[9]. Reza - Rajabi Moghaddam: "Synchronous Reluctance Machine (SynRM)in Variable Speed Drives (VSD) Applications", Doctoral Thesis, Stockholm, Sweden 2011

[10]. Jong-Bim Im, Wonho Kim, Kwangsoo Kim, Chang-Sung Jin, Jae-Hak Choi, Ju Lee: "Inductance Calculation Method of Synchronous Reluctance Motor Including Iron Loss and Cross Magnetic Saturation", IEEE Transactions on Magnetics, Vol. 45, No. 6, June, 2009.

[11]. Juha Pyrhonen, Tapani Jokinen, Valeria Hrabovcova: "Design of Rotating Electrical Machines", December 31, 2013.

[12]. Jere Kohelmainen: "Synchronous Reluctance Motor With Form Blocked Rotor", IEEE Transactions on Energy Conversion, Vol. 25, No. 2, June, 2010.

[13]. A. Stefanskyi, A. Dziechciarz, F. Chauvicourt, G. E. Sfakianakis, K. Ramakrishnan, K. Niyomsatian, M. Curti, N. Djukic, P. Romanazzi, S. Ayat, S. Wiedemann, W. Peng, S. Stipetic, "Researchers within the EU funded Marie Curie ITN project ADEPT, grant number 607361", 2013-2017.